Journal of Materials Chemistry A

ROYAL SOCIETY OF CHEMISTRY

PAPER

View Article Online
View Journal | View Issue

Cite this: J. Mater. Chem. A, 2022, 10, 10998

Instability of Ga-substituted $Li_7La_3Zr_2O_{12}$ toward metallic Li†

Chih–Long Tsai, *[a] Ngoc Thanh Thuy Tran, [b] Roland Schierholz, [a] Zigeng Liu, [a] Anna Windmüller, [a] Che-an Lin, [c] Qi Xu, [ad] Xin Lu, [ad] Shicheng Yu, [a] Hermann Tempel, [a] Hans Kungl,[a] Shih-kang Lin [bce] and Rüdiger-A. Eichel[adf]

Received 29th November 2021
Accepted 10th April 2022

DOI: 10.1039/d1ta10215j

rsc.li/materials-a

Ga-substituted $Li_7La_3Zr_2O_{12}$ (LLZO) garnet is among the most promising solid electrolytes for next-generation all-solid-state Li battery (SSLB) applications due to its very high Li-ion conductivity. However, the attempts to use Ga-substituted LLZO as a solid electrolyte for SSLBs are not yet successful. Here, the research results show that $Li_{6.4}Ga_{0.2}La_3Zr_2O_{12}$ can be reduced by Li at 25 °C when the surface of the material is properly cleaned. The experimental results suggest that Ga leached out of the garnet structure to form the Li–Ga alloy, which apparently would short-circuit the battery if Ga-substituted LLZO is used as a solid electrolyte. When low concentration Ga-substitution is applied, *e.g.* $Li_{6.45}Ga_{0.05}La_3Zr_{1.6}Ta_{0.4}O_{12}$, the material seems stable against Li at ambient temperature but not at high temperatures, where heat treatment is usually used to reduce the interfacial resistance between Li and LLZO. The experimental results are also supported by density functional theory calculations to show that the Ga-substituted LLZO/Li interface tends to transform into LLZO and the Li_2Ga intermetallic compound. The results highlight the importance of substitution selection for LLZO, for which the Ga-substituted LLZO solid electrolyte may not be suitable for direct contact with metallic Li.

Introduction

All-solid-state Li batteries (SSLBs) have been proposed as next generation electrochemical energy storage devices because of their possibility for achieving higher energy densities than nowadays Li-ion batteries (LIBs). One of the keys for SSLBs to achieve higher energy densities is by replacing the traditional graphite anode with the Li anode, which requires a solid electrolyte with high electrochemical stability toward Li. Among the various Li-ion conductors, garnet structured materials based on cubic phase $Li_7La_3Zr_2O_{12}$ (LLZO) have been considered as one of the most promising solid electrolytes due to their stability against Li, relatively high Li-ion conductivity and wide electrochemical window.[1] However, application of LLZO as the solid electrolyte for SSLBs is slow in progress due to challenges such as Li dendrite penetration through high relative density LLZO,[2] difficulties in thin LLZO film preparations,[3–7] high material processing temperatures that cause chemical instability between active electrode materials and LLZO[8,9] and internal elemental diffusion during battery fabrications.[10,11]

In the LLZO-type solid electrolytes, Ga-substituted LLZO represents one of the most studied materials due to its very high Li-ion conductivity at room temperature, >1 mS cm^{-1}, which is much higher than that for other popular substitutions such as Al or Ta.[1] The fundamental mechanism leading to this higher conductivity is not yet clear. Specifically, nuclear magnetic resonance (NMR) spectroscopy has been used to study the local environment of Ga to understand its site preference. Rettenwander *et al.* applied ultrahigh magnetic field NMR spectroscopy for studying Ga and Al co-substituted LLZO suggesting that Ga and Al have similarity in site preference in tetrahedral 24*d* and octahedral 96*h* sites.[12] It was hypothesized before that Ga is solely located on the 96*h* site irrespective of the amount of Ga-substitution, which would not interfere with the diffusion of Li-ions as opposite to the Al-substitution that occupied the 24*d* site to act as a blockade for Li-ion conduction.[13] The results weaken the previous assumption that substituent's site preference is responsible for the higher Li-ion conductivity of Ga- than Al-

[a]Institut für Energie– und Klimaforschung (IEK–9: Grundlagen der Elektrochemie), Forschungszentrum Jülich, D–52425 Jülich, Germany. E-mail: c.tsai@fz-juelich.de
[b]Hierarchical Green-Energy Materials (Hi-GEM) Research Center, National Cheng Kung University, Tainan 70101, Taiwan
[c]Department of Materials Science and Engineering, National Cheng Kung University, Tainan 70101, Taiwan
[d]Institut für Materialien und Prozesse für elektrochemische Energiespeicher– und wandler, RWTH Aachen University, D–52074 Aachen, Germany
[e]Program on Smart and Sustainable Manufacturing, Academy of Innovative Semiconductor and Sustainable Manufacturing, National Cheng Kung University, Tainan 70101, Taiwan
[f]Institut für Energie– und Klimaforschung (IEK–12: Helmholtz–Institute Münster, Ionics in Energy Storage), Forschungszentrum Jülich, D–48149 Münster, Germany

† Electronic supplementary information (ESI) available. See https://doi.org/10.1039/d1ta10215j

substituted LLZO. Furthermore, Karasulu *et al.* performed solid-state ^{17}O, ^{27}Al, and ^{71}Ga magic angle spinning (MAS) NMR spectroscopy combined with density functional theory (DFT) calculations to suggest that the sharp and broad features in ^{27}Al and ^{71}Ga NMR spectra are from the tetrahedral 24*d* site with varying local distortions, whereas the octahedral 96*h*/48*g* sites are energetically inaccessible and not experimentally observed.[14] This result is also in agreement with that of Bernuy-Lopez *et al.* from their ^{71}Ga MAS NMR study.[15]

Neutron powder diffraction (NPD) was also used for understanding the site occupation for Ga-substitution in LLZO by taking advantage of knowing that the scattering length of Ga is positive while that of Li is negative. The refinements of the NPD results are in agreement with Ga-ions being located on the tetrahedral 24*d* site while Li-ions are occupying both tetrahedral 24*d* and octahedral 96*h* sites, with more Li-ions at the 96*h* site than that at the 24*d* site.[16–18] Combining the ^{6}Li MAS NMR results, which suggests that the Li-ions at the octahedral 96*h* site have a higher mobility than those at the tetrahedral 24*d* site, and NDP results, Wu *et al.* proposed that the strong coulombic repulsion between immobile Ga-ions and the nearby Li-ions shifts Li-ions away from their central position within the octahedral 96*h* site in the garnet structure. Hence, the higher Li-ion conductivity of Ga-substituted LLZO can be attributed to the enhanced mobility of Li-ions that increased from the coulombic repulsion between Ga-ions and Li-ions.[17]

Even though LLZO is generally regarded as electrochemically stable when in contact with Li, recent research studies have discovered that the stability of LLZO toward Li is highly dependent on its substitutions. Theoretically, DFT calculations are used to determine the thermodynamic electrochemical stability window of LLZO.[19–21] The results show that the reduction decomposition of LLZO only occurred at a voltage below 0.05 V *vs.* Li/Li^+, where LLZO is reduced into Li_2O, Zr_3O and La_2O_3. When reducing the potential down to 0.004 V *vs.* Li/Li^+, Zr_3O can be further reduced into Zr metal. Furthermore, DFT calculations also suggest that small amounts of substitutions such as Al, Ta and Nb do not have large effect on the reduction potential of LLZO. Therefore, the good stability of LLZO against Li should be a result of formation of the surface passivation layer by Li_2O, La_2O and other oxides. Experimentally, Zhu *et al.* used X-ray photoelectron spectroscopy (XPS) and electrochemical impedance spectroscopy (EIS) to show the interfacial reactivity between LLZO and Li.[22] Their XPS results show that Zr^{4+} can be reduced by Li into Zr^0 or Zr^{2+} on the surface of Al-, Ta- and Nb-substituted LLZO. The formation of an "oxygen-deficient interphase" that protects Al- and Ta-substituted LLZO from further reduction into their bulk, and, therefore, stabilized the systems. In contrast, the Nb-ions in Nb-substituted LLZO have a thermodynamic preference to segregate to the interface between Nb-substituted LLZO and Li. The presence of the enhanced Nb content at the interface combined with significant reduction of Nb-ions by Li enables the reduction reaction propagation into the bulk Nb-substituted LLZO. Similarly, Rettenwander *et al.* revealed that Li-deficient tetragonal LLZO is formed when Fe-substituted LLZO is in contact with Li by using Raman spectroscopy.[23] Black surface coloration at the interface between Fe-substituted LLZO and Li can be observed due to the reduction of Fe^{3+} into Fe^{2+} in Fe-substituted LLZO.

Thin film approaches have been proposed for LLZO-type solid electrolytes in SSLB fabrications for achieving a better energy density due to the use of heavy La and Zr elements, that gives a relatively high theoretical density of ~5.3 g cm^{-3} for LLZO,[24] when compared to sulfide-, *e.g.* Li_3PS_4: 1.83 g cm^{-3},[25] phosphate-, *e.g.* LiPON: 2.30 g cm^{-3} (ref. 26) and halide-, *e.g.* Li_3InCl_6: 2.69 g cm^{-3},[27] types of solid electrolytes. However, the thin film fabrications are not as straightforward as what was expected due to Li evaporation and reaction with the used substrates at high processing temperatures as well as inability to completely crystallize the deposited precursor into the garnet structure, which leads to the reported LLZO thin films usually having Li-ion conductivities at least one order lower than that of the bulk LLZO.[3,4,7] Nevertheless, Romanyuk *et al.* were able to deposit a Ga-substituted LLZO thin film with a thickness of ~1 μm and a record high ionic conductivity of 1.9×10^{-4} S cm^{-1} at room temperature.[6] Unfortunately, demonstration of the Ga-substituted LLZO thin film as a solid electrolyte for thin film SSLBs without any assistance of a liquid electrolyte is still not yet available.[5] Although the studies of Ga-substituted LLZO had been quite popular, the report of electrochemical stability of Ga-substituted LLZO toward Li is lacking, especially the real electrochemical stability of Ga-substituted LLZO toward Li is often hidden by its surface impurities, such as Li_2CO_3, due to Li-proton exchange.[1]

Here, the electrochemical stability of Ga-substituted LLZO toward Li has been studied. The results show that the electrochemical stability of Ga-substituted LLZO toward Li is much lower than what is expected due to the leaching out of Ga into the grain boundary when in contact with Li. Especially, a low substitution of 0.05 mole Ga to the Li site also de-stabilizes LLZO at high temperatures when compared to that by using 0.05 mole Al substituent. The conclusion from the experimental results is also supported by density functional theory calculations. The results point out the importance of substituent selection when the LLZO thin film is expected to be used as a solid electrolyte for SSLB developments.

Results

The start point of looking into the chemical stability of Ga-substituted LLZO toward Li was due to the observation of short circuiting of SSLBs directly after the attachment of the Li anode to half-cells, which was fabricated by using $LiCoO_2$/$Li_{6.45}Ga_{0.05}La_3Zr_{1.6}Ta_{0.4}O_{12}$ as the composite cathode and $Li_{6.45}Ga_{0.05}La_3Zr_{1.6}Ta_{0.4}O_{12}$ as the solid electrolyte, while the same structure of SSLBs using $Li_{6.45}Al_{0.05}La_3Zr_{1.6}Ta_{0.4}O_{12}$ as the solid electrolyte does not encounter the same problem,[11] especially when the SSLBs were heated up to 250 °C for reducing the interfacial resistance between $Li_{6.45}Ga_{0.05}La_3Zr_{1.6}Ta_{0.4}O_{12}$ and Li.[28] Here, cubic phase LLZO is stabilized by substituting Ta into the Zr site. The change of low Al to Ga substitution was intended to increase the total ionic conductivity of fabricated LLZO since Ga-substituted LLZO is known to have the highest Li-ion

conductivity among the garnet structured LLZO pellets. $Li_{6.4}Ga_{0.2}La_3Zr_2O_{12}$ was further synthesized for the study of chemical stability toward Li due to its higher concentration of Ga for easier characterization and ability to compare to publications.[12–17,29–42]

Reduction reaction of Ga-substituted LLZO

After the synthesis of the materials, EIS measurements were used for determining the Li-ion conductivities of sintered $Li_{6.45}Ga_{0.05}La_3Zr_{1.6}Ta_{0.4}O_{12}$ and $Li_{6.4}Ga_{0.2}La_3Zr_2O_{12}$, as shown in Fig. S1.† Under the optimized sintering conditions, the resistance contributions from grain boundaries of both samples in the EIS measurements were able to be reduced to negligible numbers even at −60 °C. Therefore, total conductivities were calculated for both samples, for which $Li_{6.45}Ga_{0.05}La_3Zr_{1.6}Ta_{0.4}O_{12}$ and $Li_{6.4}Ga_{0.2}La_3Zr_2O_{12}$ have the total conductivities of 0.75 mS cm^{-1} and 1.48 mS cm^{-1} at 30 °C, respectively. The high total conductivities are in agreement with previous reports that indicate that the prepared samples should have similar good qualities.[17,18,29,31–33,43,44] Since the reduction reaction is a function of time, temperature or both, the reduction reactions of $Li_{6.4}Ga_{0.2}La_3Zr_2O_{12}$ and $Li_{6.45}Ga_{0.05}La_3Zr_{1.6}Ta_{0.4}O_{12}$ were carried out by attaching Li foil onto their surfaces and then placing them onto a 250 °C heating plate to visualize the reaction, and monitored by EIS at room temperature for long term stability tests.

Fig. 1(a) shows photos of the reduction reaction of $Li_{6.4}Ga_{0.2}La_3Zr_2O_{12}$ by using Li after placing it onto a 250 °C heating plate. It can be clearly seen that the colour of $Li_{6.4}Ga_{0.2}La_3Zr_2O_{12}$ turned from ivory to black from the interface of Li/$Li_{6.4}Ga_{0.2}La_3Zr_2O_{12}$ and propagated through the whole 1.5 cm thick pellet, also see movie S1.†

The Li stripe on top of $Li_{6.4}Ga_{0.2}La_3Zr_2O_{12}$ indicates that the reduction reaction starts at a temperature lower than the melting temperature of Li, *i.e.* 180.5 °C. In contrast, $Li_{6.45}Al_{0.05}La_3Zr_{1.6}Ta_{0.4}O_{12}$ did not show any visible change of colour or reaction throughout the experiment. For $Li_{6.45}Ga_{0.05}La_3Zr_{1.6}Ta_{0.4}O_{12}$, the reduction reaction is much slower than that of $Li_{6.4}Ga_{0.2}La_3Zr_2O_{12}$. Fig. 1(b) shows photos of the results from heating Li/LLZO/Li symmetric cells of $Li_{6.45}Al_{0.05}La_3Zr_{1.6}Ta_{0.4}O_{12}$ and $Li_{6.45}Ga_{0.05}La_3Zr_{1.6}Ta_{0.4}O_{12}$ at 250 °C for 45 minutes. Both the pellets have a thickness of 0.6 mm. After removing the Li electrodes inside a glove box, the $Li_{6.45}Ga_{0.05}La_3Zr_{1.6}Ta_{0.4}O_{12}$ pellet was also found in black colour while a small part of the material at the central part of the pellet remained ivory in color. This indicates that the reduction reaction of $Li_{6.45}Ga_{0.05}La_3Zr_{1.6}Ta_{0.4}O_{12}$ is much slower than that of $Li_{6.4}Ga_{0.2}La_3Zr_2O_{12}$ but still not stable towards Li. On the other hand, $Li_{6.45}Al_{0.05}La_3Zr_{1.6}Ta_{0.4}O_{12}$ showed only a thin layer of coloration, which can be explained by the reduction of Zr^{4+} to Zr^{2+} to form a stable

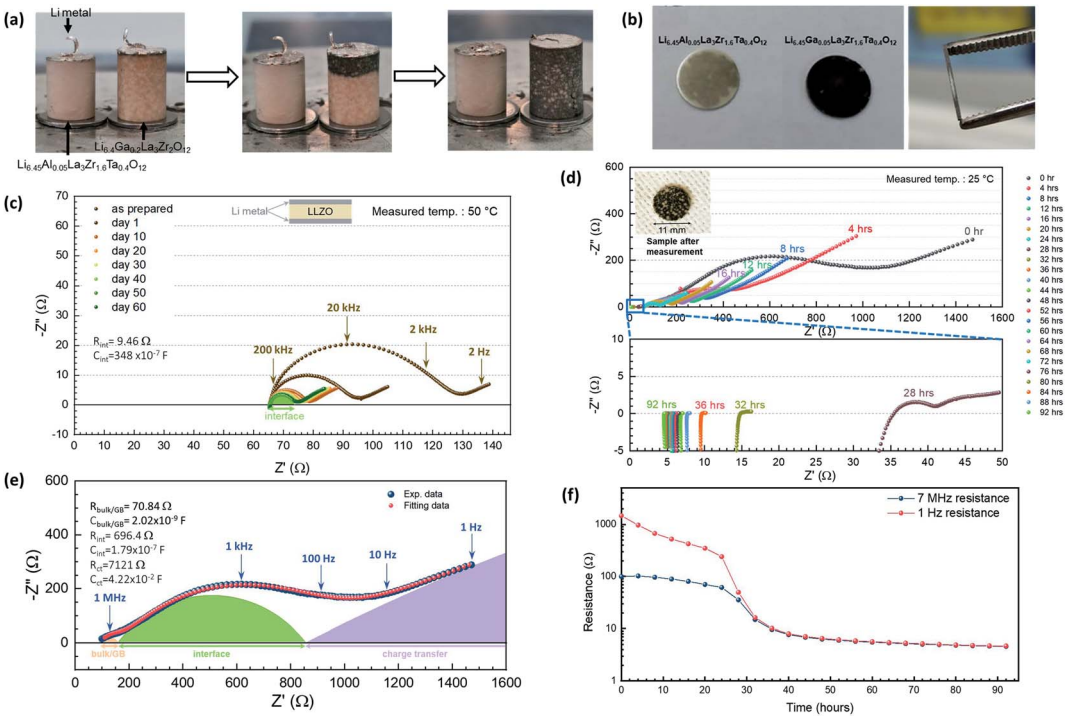

Fig. 1 Reduction reaction of Ga-substituted LLZO (a) photos of the reduction reaction of $Li_{6.4}Ga_{0.2}La_3Zr_2O_{12}$ after placing on a 250 °C heating plate while $Li_{6.45}Al_{0.05}La_3Zr_{1.6}Ta_{0.4}O_{12}$ exhibits no noticeable reaction. (b) Photos of the reduced $Li_{6.45}Ga_{0.05}La_3Zr_{1.6}Ta_{0.4}O_{12}$ pellet after immersing into 250 °C molten Li while $Li_{6.45}Al_{0.05}La_3Zr_{1.6}Ta_{0.4}O_{12}$ only shows slight discoloration (left) and cross-section of the reduced $Li_{6.45}Ga_{0.05}La_3Zr_{1.6}Ta_{0.4}O_{12}$ pellet (right). EIS measurements for the long term stability test of (c) $Li_{6.45}Ga_{0.05}La_3Zr_{1.6}Ta_{0.4}O_{12}$ and (d) $Li_{6.4}Ga_{0.2}La_3Zr_2O_{12}$. (e) Nyquist plot and (f) cell resistance of Li/$Li_{6.4}Ga_{0.2}La_3Zr_2O_{12}$/Li symmetric cell.

oxygen-deficient interphase layer to block the continuous reduction reaction within $Li_{6.45}Al_{0.05}La_3Zr_{1.6}Ta_{0.4}O_{12}$.[22]

The electrochemical stabilities of $Li_{6.45}Ga_{0.05}La_3Zr_{1.6}Ta_{0.4}O_{12}$ and $Li_{6.4}Ga_{0.2}La_3Zr_2O_{12}$ toward Li were also examined at 50 °C and 25 °C, respectively, by using EIS for monitoring the reactions. The surfaces of the LLZO pellets were polished in a glove box to remove any possible Li_2CO_3/LiOH layer from Li-proton exchange before Li electrodes were attached to the pellets. Isostatic pressing with a pressure of 500 MPa and 30 second dwell time was used to reinforce the attachment of Li electrodes onto LLZO pellets after Li electrodes were attached onto LLZO by hand. However, short circuiting of $Li_{6.4}Ga_{0.2}La_3Zr_2O_{12}$ symmetric cells was always observed right after pressing. After removal of Li electrodes, black surface coloration can be seen in some parts of the $Li_{6.4}Ga_{0.2}La_3Zr_2O_{12}$ pellets, as shown in Fig. S2.†

The short circuiting of the $Li_{6.4}Ga_{0.2}La_3Zr_2O_{12}$ symmetric cells shows the importance of proper surface cleaning to see the reduction reaction of $Li_{6.4}Ga_{0.2}La_3Zr_2O_{12}$ from Li. Nevertheless, Li electrodes were hand pressed onto $Li_{6.4}Ga_{0.2}La_3Zr_2O_{12}$ pellets for the experiment. Fig. 1(c) shows the long term stability test of $Li_{6.45}Ga_{0.05}La_3Zr_{1.6}Ta_{0.4}O_{12}$ against Li at 50 °C for 60 days. The as prepared symmetric cell has a bulk resistance of ~65 Ω and interface resistance of ~32 Ω at 50 °C. With the increase of time at 50 °C, the interface resistance reduced from ~32 Ω to only ~4.7 Ω while the bulk resistance remained the same at ~65 Ω. The decrease of the interface resistance can be explained by the improvement of the contact between Li and $Li_{6.45}Ga_{0.05}La_3Zr_{1.6}Ta_{0.4}O_{12}$ due to Li deposition/dissolution during the EIS measurements and the possible surface reaction between Li and $Li_{6.45}Ga_{0.05}La_3Zr_{1.6}Ta_{0.4}O_{12}$. It could be understood that an electric current of ~150 μA cm^{-2} or higher was sent between the Li electrodes when a 20 mV AC bias was used in the EIS measurements. Li can be deposited/stripped onto/from the interface for improving the contact resistance especially when the measuring frequency was 1 Hz. Since the bulk resistance and the colour of the surface remained the same after the measurements, the surface reaction between Li and $Li_{6.45}Ga_{0.05}La_3Zr_{1.6}Ta_{0.4}O_{12}$ is unlikely to happen at 50 °C but cannot be eliminated completely at the nanoscale.

Fig. 1(d) shows the EIS measurement of the prepared Li/$Li_{6.4}Ga_{0.2}La_3Zr_2O_{12}$ /Li symmetric cell at 25 °C by using 1 mm thick $Li_{6.4}Ga_{0.2}La_3Zr_2O_{12}$ pellet. The EIS spectrum of the as prepared cell can be fit by using a circuit consisting of one resistor in series with three other R-CPE circuits. It is important to mention again that the separation of the bulk and grain boundary contributions was challenging even when ultra-high frequency EIS and ultra-low temperatures were used for the measurement, as shown in Fig. S1.† Hence, the assignment of one of the R-CPE circuits with $C = 2.02 \times 10^{-9}$ F solely to the contribution from the grain boundary would not be convincing. Therefore, the contributions from three different R-CPE circuits were assigned to the bulk/grain boundary of LLZO ($C_{bulk/GB} = 2.02 \times 10^{-9}$ F), interface resistance ($C_{int} = 1.79 \times 10^{-7}$ F) and charge transfer ($C_{ct} = 4.22 \times 10^{-2}$ F), where the total resistance of the $Li_{6.4}Ga_{0.2}La_3Zr_2O_{12}$ solid electrolyte was ~160 Ω, *i.e.* the resistance (Z') from $x = 0$ to the intercept at low frequency for the $R_{bulk/GB}$–$C_{bulk/GB}$ circuit, as shown in Fig. 1(e). The interface resistance was ~348 Ω, which is much higher than that of the $Li_{6.45}Ga_{0.05}La_3Zr_{1.6}Ta_{0.4}O_{12}$ cell (~32 Ω) because the attachment of Li electrodes was only done by hand. With the increase of time, all the three contributions that were recognized from fitting were dramatically reduced, as shown in Fig. 1(d). After 32 hours, the contributions from the interface and charge transfer were no more recognizable, while the resistance from the $Li_{6.4}Ga_{0.2}La_3Zr_2O_{12}$ pellet was reduced to ~15 Ω only. If we take the real part of EIS spectra at 7 MHz as the bulk resistance contributions from the $Li_{6.4}Ga_{0.2}La_3Zr_2O_{12}$ pellet solely and 1 Hz as the total cell resistance, which includes the bulk resistance and interface resistances of the cell, it can be seen that the cell resistance decreased much faster than that for the bulk $Li_{6.4}Ga_{0.2}La_3Zr_2O_{12}$ pellet solely in the first 32 hours. This indicates that the reduction reaction of the $Li_{6.4}Ga_{0.2}La_3Zr_2O_{12}$ pellet by Li electrodes starts from the surfaces into the bulk and finally stabilized to ~5 Ω for the whole cell, Fig. 1(f). After the measurements, $Li_{6.4}Ga_{0.2}La_3Zr_2O_{12}$ was black in colour throughout the pellet with some ivory colour single crystals decorated on the pellet, as shown in the inset picture in Fig. 1(d). The small cell resistance and the colour change of the pellet both indicate that the reduction reaction of $Li_{6.4}Ga_{0.2}La_3Zr_2O_{12}$ by Li can happen at room temperature.

Crystal structure analysis

The phase compositions of pristine and reduced samples were examined by XRD. The diffraction pattern of $Li_{6.4}Ga_{0.2}La_3Zr_2O_{12}$ can be described by a cubic garnet phase in space group $Ia\bar{3}d$, as shown in Fig. 2(a). The lattice parameter was refined to be a = 12.970 Å. $Li_{6.45}Ga_{0.05}La_3Zr_{1.6}Ta_{0.4}O_{12}$ can be fitted reasonably by using a composition of a cubic garnet phase, $Ia\bar{3}d$ (a = 12.934 Å), and a tetragonal phase, $I4_1acd$, Fig. 2(c). No impurity phase was detected within the sensitivity limitation of XRD. After the reduction, the diffraction pattern of $Li_{6.4}Ga_{0.2}La_3Zr_2O_{12}$ remains majorly unchanged. The cubic main phase is maintained and the peaks only shift slightly to lower angles, indicating an increase in the lattice parameter (a = 12.974 Å). Additionally, the highest reflections show clear asymmetry/shoulders on the low angle side. The positions of these shoulders match with the tetragonal garnet phase, $I4_1acd$. A reasonable fit was achieved by fitting cubic phase $Ia\bar{3}d$ and tetragonal phase $I4_1acd$ to the diffraction pattern for the reduced $Li_{6.4}Ga_{0.2}La_3Zr_2O_{12}$, as shown in Fig. 2(b). The reduced $Li_{6.45}Ga_{0.05}La_3Zr_{1.6}Ta_{0.4}O_{12}$ XRD pattern shows significant line broadening when compared to that of the pristine $Li_{6.45}Ga_{0.05}La_3Zr_{1.6}Ta_{0.4}O_{12}$. One explanation could be that the crystallinity of reduced $Li_{6.45}Ga_{0.05}La_3Zr_{1.6}Ta_{0.4}O_{12}$ is lower than that of the pristine one. However, fitting cubic $Ia\bar{3}d$ garnet to the diffraction pattern of the reduced sample while refining the parameters for line broadening from it (size and strain) left significant intensity contribution that remained unfitted, as shown in Fig. S3(a).† A more reasonable fit was achieved with the tetragonal phase $I4_1acd$, with line broadening effects from the size and strain, as shown in Fig. 3(b). This means that the observed line broadening from the pristine sample to the

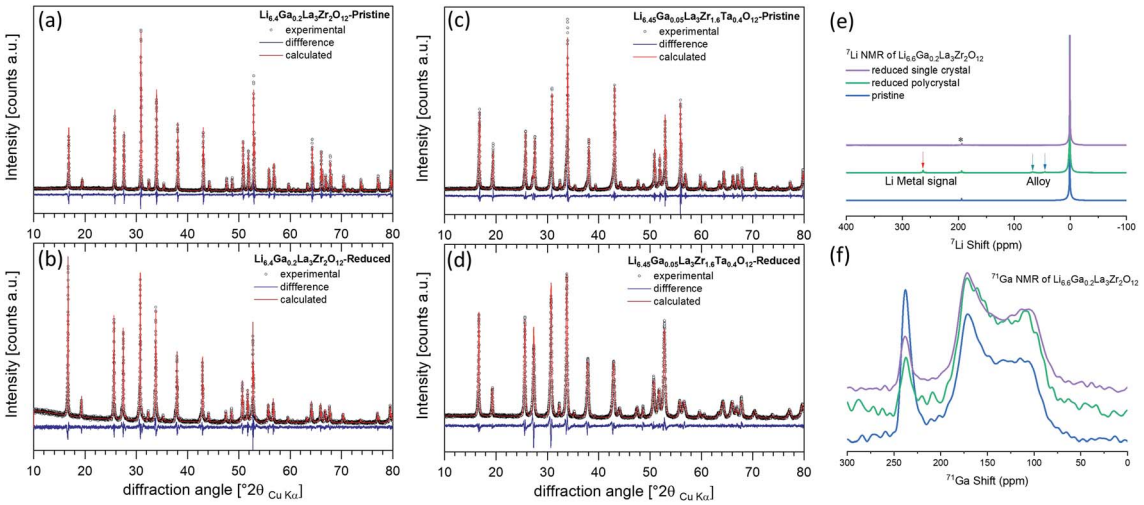

Fig. 2 XRD refinement of (a) pristine and (b) reduced $Li_{6.4}Ga_{0.2}La_3Zr_2O_{12}$, and (c) pristine and (d) reduced $Li_{6.45}Ga_{0.05}La_3Zr_{1.6}Ta_{0.4}O_{12}$. (e) ^7Li and (f) ^{71}Ga MAS NMR spectra of pristine and reduced $Li_{6.4}Ga_{0.2}La_3Zr_2O_{12}$. Asterisks indicate the spinning side band.

reduced sample can be understood as a superimposition of peak splitting from the tetragonal phase plus line broadening effects due to reduced crystallinity of the sample. Note that the difference plot shown in Fig. 2(d) still indicates that intensities of the highest reflections remain unfitted. This could be an effect of the inhomogeneous size distribution or a small fraction of the cubic phase that is superimposed by the tetragonal phase. The structure of reduced $Li_{6.45}Ga_{0.05}La_3Zr_{1.6}Ta_{0.4}O_{12}$ changes from a majorly cubic phase to a complete tetragonal phase indicating that the Li concentration within reduced $Li_{6.45}Ga_{0.05}La_3Zr_{1.6}Ta_{0.4}O_{12}$ increases to more than 6.6, which would require at least one other element than Ga in $Li_{6.45}Ga_{0.05}La_3Zr_{1.6}Ta_{0.4}O_{12}$ to reduce its valence for the uptaking of the extra Li-ions and maintain the whole system neutral.[45]

^7Li and ^{71}Ga MAS NMR spectra were used for characterizing the pristine and reduced $Li_{6.4}Ga_{0.2}La_3Zr_2O_{12}$. The samples were collected from the central part of the 1.5 cm thick pellet to avoid any possible residual Li electrode for the MAS NMR measurements. The ^7Li MAS NMR spectrum of pristine $Li_{6.4}Ga_{0.2}La_3Zr_2O_{12}$, Fig. 2(e), shows one resonance at 1.2 ppm, which can be assigned to the Li-ions in the two Li sites with a fast exchanging rate in $Li_{6.4}Ga_{0.2}La_3Zr_2O_{12}$. Apart from the ^7Li resonance of $Li_{6.4}Ga_{0.2}La_3Zr_2O_{12}$, 3 new resonances were observed in the ^7Li

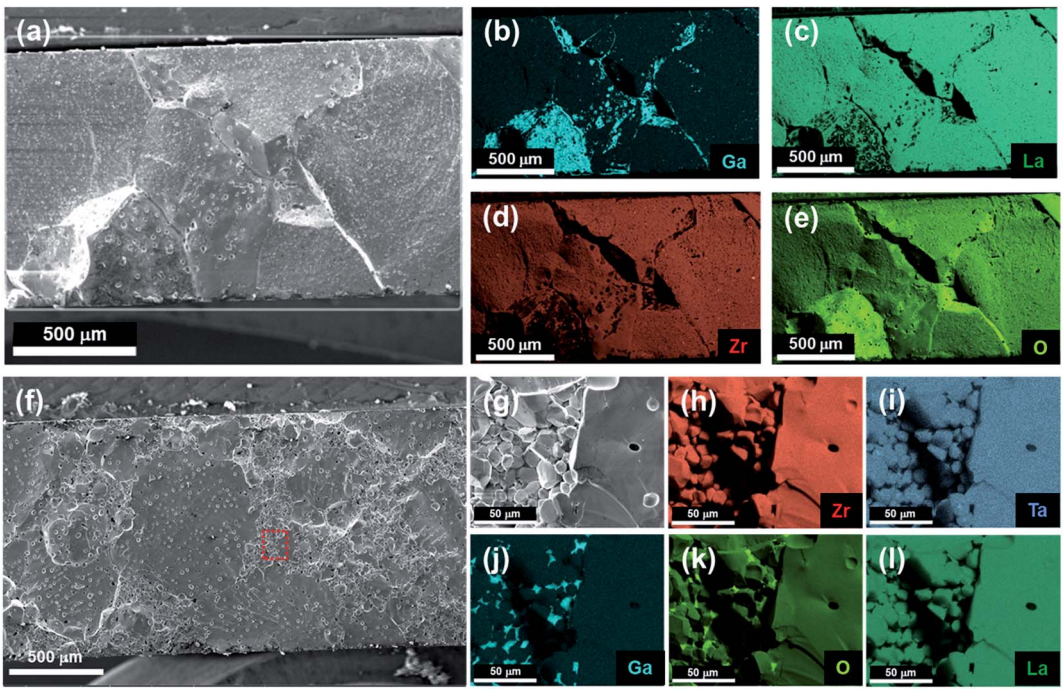

Fig. 3 Microstructure and EDS mapping images of pristine $Li_{6.4}Ga_{0.2}La_3Zr_2O_{12}$, (a)–(e), and $Li_{6.45}Ga_{0.05}La_3Zr_{1.6}Ta_{0.4}O_{12}$, (f)–(l).

MAS NMR spectrum of the reduced $Li_{6.4}Ga_{0.2}La_3Zr_2O_{12}$ polycrystalline sample. The far left one at 263.2 ppm is assigned to the Li metal signal and the two middle resonances at 67.2 and 45.8 ppm, respectively, are tentatively assigned to the Li–Ga alloy. The result indicates that Li metal was infiltrated into the pellet and reacted with Ga to form the alloy. Furthermore, 2D exchange spectroscopy (EXSY) experiments were performed for the reduced $Li_{6.4}Ga_{0.2}La_3Zr_2O_{12}$ sample. Only diagonal peaks were observed for Li metal and $Li_{6.4}Ga_{0.2}La_3Zr_2O_{12}$ resonances, while off-diagonal peaks were obtained for the Li–Ga alloy resonances with the mixing time between 1 and 30 ms, as shown in Fig. S4,† implying that the two alloy signals are exchanged at the millisecond timescale. The exchange rate determined by fitting the cross peak build up curve is 8.9 s^{-1} at 295 K. Thus, the ^{7}Li MAS NMR spectrum suggests that the Li–Ga alloy is likely the pathway for Li metal to penetrate into $Li_{6.4}Ga_{0.2}La_3Zr_2O_{12}$. For the reduced single crystal samples, collected by cleaning out the black color material using absolute ethanol, as shown in Fig. S2(b),† only the Li-ion signal of $Li_{6.4}Ga_{0.2}La_3Zr_2O_{12}$ can be detected in the ^{7}Li MAS NMR spectrum, suggesting that the infiltration of metallic Li occurs only along the grain boundaries instead of in closed porosities within the crystals. ^{71}Ga MAS NMR spectra of pristine and reduced $Li_{6.4}Ga_{0.2}La_3Zr_2O_{12}$ samples, as shown in Fig. 2(f), show two resonances: one sharp resonance at ~238 ppm is assigned to Ga-ions at the ordered tetragonal 96*h* site and the broad resonance between 50 ppm and 200 ppm is assigned to Ga-ions at the distorted tetragonal 24*d* site within $Li_{6.4}Ga_{0.2}La_3Zr_2O_{12}$.[12–15,37] When compared with the pristine sample, the reduced $Li_{6.4}Ga_{0.2}La_3Zr_2O_{12}$ shows relatively less Ga-ions in the ordered tetragonal 96*h* site, implying that some of the Ga was leached out of the garnet structure during the reduction process. It has to be emphasized again that the chemical shift from the ^{71}Ga MAS NMR spectrum directly points to the Ga-ions in the garnet structured $Li_{6.4}Ga_{0.2}La_3Zr_2O_{12}$ without influence of the impurity phase at grain boundaries.

Microstructure and chemical distribution analysis

The microstructures of $Li_{6.4}Ga_{0.2}La_3Zr_2O_{12}$ and $Li_{6.45}Ga_{0.05}La_3Zr_{1.6}Ta_{0.4}O_{12}$ from the SEM images along with their EDS elemental mapping images are shown in Fig. 3. The compact microstructures indicate that both samples have high relative densities after the sintering process. For $Li_{6.4}Ga_{0.2}La_3Zr_2O_{12}$, abnormal grain growth was observed for the sintered pellet, as shown in Fig. 3(a). Grains as big as 1 mm in diameter can be obtained, which corresponds to the visible particles in the optical pictures of the pristine or reduced $Li_{6.4}Ga_{0.2}La_3Zr_2O_{12}$ pellets, as shown in Fig. 1(a) and (d). From the EDS elemental mapping images, the homogeneous distribution of La and Zr within the grains presents that the grinding and calcination processes during the solid state reaction were properly done for material homogenization. However, a Ga-rich phase can be found at the grain boundaries, *i.e.* grain surfaces when an intergranular crack is present, where the oxygen concentration was also found to be higher than that within the grains. It is worth mentioning that the observed Ga-rich phase covering the surface of the grains and the higher atomic percentage of Ga, *e.g.* 25 at% of Ga for $LiGaO_2$ *vs.* 0.8 at% of Ga for $Li_{6.4}Ga_{0.2}La_3Zr_2O_{12}$, make it more observable when performing EDS mapping. Nevertheless, the observations of the cubic phase of $Li_{6.4}Ga_{0.2}La_3Zr_2O_{12}$ from XRD measurement, very high total Li-ion conductivity and Ga-substitution into 96*h* and 24*d* Li-sites from NMR measurement provide direct evidence of successful substitution of Ga into the garnet structured LLZO. Since $LiGaO_2$ is often seen as the secondary phase in Ga-substituted LLZO, the observed Ga and oxygen rich secondary phase could be $LiGaO_2$.[5,6,13,30,34–36,43,46] The microstructure of $Li_{6.45}Ga_{0.05}La_3Zr_{1.6}Ta_{0.4}O_{12}$ appears to be bimodal, where large grains can be as big as 500 μm with small grains of sizes of about 10 μm fitted between the large grains, as shown in Fig. 3(f). The effect of Ga substitution into Li sites for $Li_{6.45}Ga_{0.05}La_3Zr_{1.6}Ta_{0.4}O_{12}$ can be clearly seen from the microstructure when compared to $Li_{6.45}Al_{0.05}La_3Zr_{1.6}Ta_{0.4}O_{12}$, as shown in Fig. S5,† which consist of much smaller grains with a more homogeneous grain size distribution ranging from 10 to 50 μm that is in agreement with the studies by Buannic *et al.* and Lan *et al.*[33,37] EDS mapping images of $Li_{6.45}Ga_{0.05}La_3Zr_{1.6}Ta_{0.4}O_{12}$ shows similar results to that of $Li_{6.4}Ga_{0.2}La_3Zr_2O_{12}$, as shown in Fig. 3(h)–(l). La, Zr and Ta are homogeneously distributed within the material while a Ga and oxygen rich secondary phase was found on the grain boundary. The formation of $LiGaO_2$ on the grain boundaries for both $Li_{6.4}Ga_{0.2}La_3Zr_2O_{12}$ and $Li_{6.45}Ga_{0.05}La_3Zr_{1.6}Ta_{0.4}O_{12}$ indicates that the substitution of Ga into LLZO was not completed for both materials, even though heat treatments at high temperatures and long dwell times during the solid state reaction were applied, *i.e.* one calcination step at 850 °C for 20 hours and two individual calcination steps at 1000 °C for 20 hours and a final sintering step at 1175 °C for 30 hours.

Fig. 4 shows the microstructures of reduced $Li_{6.4}Ga_{0.2}La_3Zr_2O_{12}$ and $Li_{6.45}Ga_{0.05}La_3Zr_{1.6}Ta_{0.4}O_{12}$. The material with dark contrast in the BSE micrograph, *i.e.* light molar mass elements, fills up the grain boundaries and covers most of the grains of reduced $Li_{6.4}Ga_{0.2}La_3Zr_2O_{12}$, as shown in Fig. 4(a). It is important to note that new cracks were formed and cut through the grains of $Li_{6.4}Ga_{0.2}La_3Zr_2O_{12}$. These newly developed cracks were also filled up with the material of dark contrast, which suggests that the gains of $Li_{6.4}Ga_{0.2}La_3Zr_2O_{12}$ were opened up by the formation of this dark contrast material. EDS mapping images were also used for identifying the elemental distributions of reduced $Li_{6.4}Ga_{0.2}La_3Zr_2O_{12}$, as shown in Fig. 4(b)–(g). Nitrogen was specifically found on the gain boundary where the dark contrast material is located, as shown in Fig. 4(c), indicating that the dark contrast material is Li_3N that was formed during transferring the reduced sample into the SEM chamber. More importantly, areas with high Ga concentration were not only found at the grain boundaries but also in the closed pores of $Li_{6.4}Ga_{0.2}La_3Zr_2O_{12}$ grains where the oxygen concentration was detected to be minimum. The observation indicates that Ga was leached out of the garnet structure as metal during the reduction process as suggested by the NMR result. Since the alloying of Ga and Li is accompanied by volume expansion, it could be understood that the newly formed transgranular

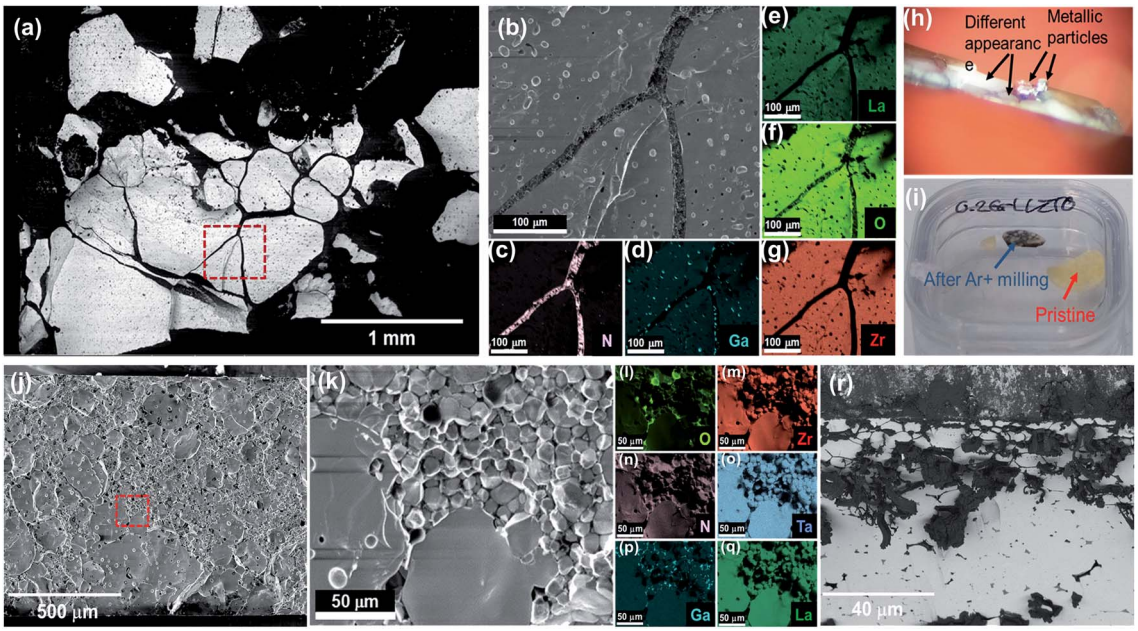

Fig. 4 Microstructure and EDS mapping image of reduced $Li_{6.4}Ga_{0.2}La_3Zr_2O_{12}$, (a)–(g). (h) Li metal expulsion and (i) reduction by Ar-ion milling of $Li_{6.4}Ga_{0.2}La_3Zr_2O_{12}$. The Microstructure and EDS mapping image of reduced $Li_{6.45}Ga_{0.05}La_3Zr_{1.6}Ta_{0.4}O_{12}$, (j)–(q). (r) Li_3N grows out of the grain boundaries from reduced $Li_{6.45}Ga_{0.05}La_3Zr_{1.6}Ta_{0.4}O_{12}$ after being exposed to air.

cracks could be a result of the Li–Ga alloy formation, which also provides the pathways for Li to infiltrate into the $Li_{6.4}Ga_{0.2}La_3Zr_2O_{12}$ pellet to keep the reduction reaction propagating through the whole ceramic pellet as suggested by the 2D EXSY result. Furthermore, the reduction reaction of $Li_{6.4}Ga_{0.2}La_3Zr_2O_{12}$ accompanied with Li metal expulsion was also observed during sample preparation for SEM by using Ar-ion milling under vacuum, as shown in Fig. 4(h) and (i). It was reported that the electron beam expulsed Li out of $Li_{6.4}La_3Zr_{1.4}Ta_{0.6}O_{12}$ during the SEM investigation due to electron injection into the bulk LLZO.[47] However, the positive charge of the Ar-ion beam and inert nature of Ar make the reason for Li metal expulsion unclear. From the change of $Li_{6.4}Ga_{0.2}La_3Zr_2O_{12}$ colour after Ar-ion milling, it could be speculated that the valence of some elements in $Li_{6.4}Ga_{0.2}La_3Zr_2O_{12}$ changed to a lower state while Li-ions need to be expelled as Li metal to keep the system neutral.

Different from $Li_{6.4}Ga_{0.2}La_3Zr_2O_{12}$, the microstructure of reduced $Li_{6.45}Ga_{0.05}La_3Zr_{1.6}Ta_{0.4}O_{12}$ did not have any noticeable change from that of the pristine one. No newly developed transgranular cracks can be found within the investigated sample cross-section. The grain boundaries of reduced $Li_{6.45}Ga_{0.05}La_3Zr_{1.6}Ta_{0.4}O_{12}$ are tightly binding the grains to hold the whole structure of the sintered pellet even after the pellet was immersed into water, as shown in Fig. S2(c).† EDS mapping images of the reduced $Li_{6.45}Ga_{0.05}La_3Zr_{1.6}Ta_{0.4}O_{12}$ pellet show similar results as that of $Li_{6.4}Ga_{0.2}La_3Zr_2O_{12}$, as shown in Fig. 4(k)–(q). Areas with higher oxygen concentration can be found, which are overlapped with higher nitrogen concentration areas. The high oxygen and nitrogen concentration also indicate that Li was infiltrated into the sample along the grain boundaries, which is in agreement with the Ar-ion polished sample that Li_3N was grown out of the reduced $Li_{6.45}Ga_{0.05}La_3Zr_{1.6}Ta_{0.4}O_{12}$ from the grain boundaries after exposing to air, as shown in Fig. 4(r). Unlike the reduced $Li_{6.4}Ga_{0.2}La_3Zr_2O_{12}$ sample, high Ga concentration was not found in the close pores within the large grains and the areas where Li was infiltrated are not always superposed with $LiGaO_2$. The result suggests that the infiltration paths for Li may not necessarily always go along with where $LiGaO_2$ is.

Density functional theory calculations

To further examine the instability of Ga-substituted LLZO toward Li metal, interfacial stability simulation by means of DFT calculations has been utilized. Reaction energies (E_r) of Ga-substituted LLZO and Li against their possible competing phases can be calculated as follows:

$$E_r(x) = E_f[\text{competing phases}] - xE_f[\text{Ga–LLZO}] - (1-x)E_f[\text{Li}]$$

where E_f[Ga–LLZO], E_f[Li], and E_f [competing phases] are formation energies of Ga-substituted LLZO, body-centred cubic phase Li, and their possible competing phases (listed in Table S1†), while x is the mole fraction of Ga-substituted LLZO to Li ($0 \leq x \leq 1$) at the interface. The reaction energy, $E_r(x)$, represents the thermodynamic contact stability of the Ga-substituted LLZO/Li interface with a specific interface composition, x, as shown in Fig. 5(a) and (b) for $Ga_{0.25}$LLZO/Li and $Ga_{0.125}$LLZO/Li, respectively.

Based on the assumption of local equilibrium at the interface,[48] the tie lines on the convex hull of $Ga_{0.25}$LLZO/Li connect the stable sets of competing phases that are marked as points

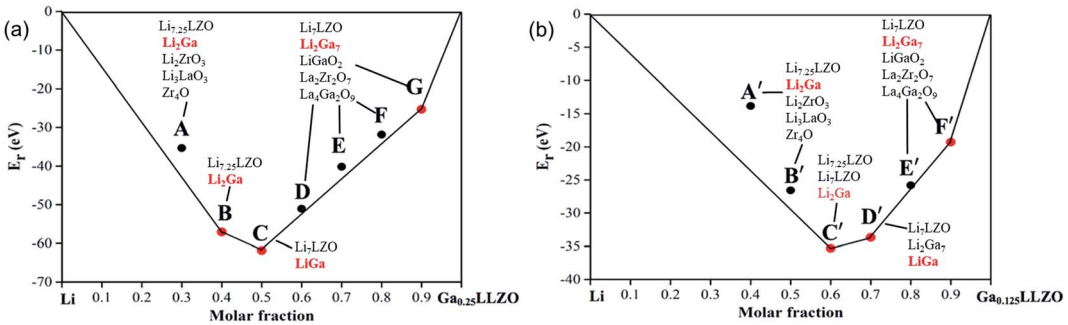

Fig. 5 The convex hulls of (a) $Ga_{0.25}LLZO$/Li and (b) $Ga_{0.125}LLZO$/Li pseudo-binary systems, in which the most stable phase constituents (those with the lowest reaction energies) at various interface compositions marked as A–D and A′–C′ are listed. The detailed interfacial reaction equations can be found in Tables S2 and S3.†

(A, B, C and D), while those above the hull are metastable at the interface of $Ga_{0.25}LLZO$/Li. Obviously, the $Ga_{0.25}LLZO$/Li interface is unstable and interfacial reactions may occur. A number of Li–Ga binary compounds may be formed at the interface, namely Li_2Ga, LiGa, and Li_2Ga_7, indicating the driving force of Ga segregation and diffusion from $Ga_{0.25}LLZO$ to the interface to react with Li. On the other hand, the interfacial reaction also drives Li atoms to diffuse from the bulk Li to the interface and transfer into Li-ions to intercalate into the garnet structure to form tetragonal phase LLZO. Among the stable interfacial phase constituents, the most energetically favourable set of competing phases in the convex hull (point A) suggests that the $Ga_{0.25}LLZO$/Li interface tends to transform into $Li_7La_3Zr_2O_{12}$ and the Li_2Ga intermetallic compound. The formation of Li_2Ga intermetallic compound also gives the reason that the reduction reaction can propagate through the whole pellet and allows the infiltration of metallic Li into the bulk. A similar result was obtained in the case of lower Ga-substitution ($Ga_{0.125}LLZO$) as shown in Fig. 5(b); however, the reaction energies are less negative. This indicates that despite being an unstable interface, its interfacial stability against metallic Li is better than the higher Ga-concentration substitution one, which is in agreement with the observation that $Li_{6.45}Ga_{0.05}La_3Zr_{1.6}Ta_{0.4}O_{12}$ is more stable toward Li than $Li_{6.4}Ga_{0.2}La_3Zr_2O_{12}$. It is worth mentioning that both $Ga_{0.25}LLZO$ and $Ga_{0.125}LLZO$ themselves are not in the ground state and could decompose when presuming that $Li_7La_3Zr_2O_{12}$ is a stable phase against Li for the calculations. The negative formation energy of $Ga_{0.25}LLZO$ and $Ga_{0.125}LLZO$ may also explain the experimental observation of $LiGaO_2$ formation on the grain boundaries. The calculated results agree closely with experimental observation on the instability of Ga-substituted LLZO against Li metal, as shown in Fig. 1 and 3.

Discussion

Owing to its very high Li-ion conductivity, Ga-substituted LLZO has been widely studied as a promising solid electrolyte for SSLB application and to understand the origin of its high Li-ionic conductivity.[12–17,29–43] However, the stability of Ga-substituted LLZO toward Li has rarely been discussed. After surveying the literature, only Chen *et al.*[31] and Su *et al.*[43] mentioned that the reactivity of Ga-substituted LLZO toward Li with the observation of crack formation after the Ga-substituted LLZO pellets were immersed in molten Li–Sn and Li, respectively. Both of them explained that the crack formation was due to the high stress generation from uptake of extra Li-ions at grain boundaries. By using EIS measurements, Pesci *et al.* reported that the resistances associated with grain boundaries and interfaces of their Li/$Li_{6.55}Ga_{0.15}La_3Zr_2O_{12}$ /Li symmetric cell were decreased after the cell assembly.[42] The reason for the decrease of cell resistances was not clear but was attributed to the improvement of interface contact or possibility of higher ionically conductive interphase formation. Publications using the Li/Ga-substituted LLZO/Li symmetric cell for EIS measurements can also be found.[15,17,36] However, their high interfacial resistances, which are usually in couple of thousand ohms, indicate that the formation of Li_2CO_3 or other impurities could protect the material from being reduced by Li during the measurements.

Here, the stability of Ga-substituted LLZO toward Li has been studied. The results show that Ga-substituted LLZO has relatively low stability when in contact with Li, even with a very low concentration substitution of Ga, *i.e.* $Li_{6.45}Ga_{0.05}La_3Zr_{1.6}Ta_{0.4}O_{12}$. It could dramatically reduce the stability of the whole system when compared to that of the Al-substituted one, *i.e.* $Li_{6.45}Al_{0.05}La_3Zr_{1.6}Ta_{0.4}O_{12}$. The reduction reaction was also found to be accompanied with the infiltration of Li into the bulk pellet along the grain boundaries. Since the reduction reaction was done without applying any external field, the infiltration of Li into the bulk pellets must be driven by the alloying effect with another element to keep Li in the metal form. From the EDS results, one possibility to create this pathway would be the reaction of $LiGaO_2$ at the grain boundaries with Li to form the Li–Ga alloy and Li_2O, where the Li–Ga alloy can keep the reaction continuing through the bulk pellet, also see ESI, Fig. S5 and movie S2† for more discussion. However, the reaction between $LiGaO_2$ and Li is not able to explain the results from ^{71}Ga MAS NMR spectroscopy that suggest that the Ga concentration in $Li_{6.4}Ga_{0.2}La_3Zr_2O_{12}$ was less than that of the pristine one and the XRD results suggest that the phase of Ga-substituted LLZO was changed from cubic to the tetragonal phase after the

reduction reaction. In combination with the results from NMR spectroscopy, XRD and EDS mapping, especially the observation of high Ga concentration in the close pores of reduced $Li_{6.4}Ga_{0.2}La_3Zr_2O_{12}$ grains, it is reasonable to conclude that Ga leaches out of Ga-substituted LLZO to form the Li–Ga alloy while some Li atoms must oxidize to form Li-ions to fill into the Li-vacancies in LLZO to keep the material neutral when Ga-substituted LLZO is in contact with Li and considering that trivalent diffusion is possible within the oxide framework.[49,50] The observed results are in good agreement with DFT calculations on the Ga-LLZO/Li interfacial stability. The leached out Ga further forms alloy with Li to keep the reduction reaction propagate through the bulk pellet by keeping its electrochemical potential the same as that of the Li electrode on the surface of the LLZO pellet due to the high electronic conductivity of the Li–Ga alloy. With the increase of the Li concentration in the garnet structure, a phase transformation from the cubic to tetragonal phase garnet structure can be expected when the Li-ion concentration in the garnet structure is higher than 6.6.[45] Nevertheless, if only considering the short circuiting of the pellet, the contribution from the reaction of $LiGaO_2$ and Li at the grain boundaries to form the Li–Ga alloy cannot be totally excluded. A similar leaching out behaviour of Al to $LiCoO_2$ to form a highly resistant tetragonal phase from cubic phase Al-substituted LLZO was reported by Park *et al.*[10] The transformation behaviour from cubic phase Fe-substituted LLZO into tetragonal phase Fe-substituted LLZO due to the reduction of Fe^{3+} to Fe^{2+} when in contact with Li was also reported by Rettenwander *et al.*[23] Similarly, the observation of the reduction reaction of LLZO from Li to form a black surface coloration layer was reported for Fe-, Nb- and (Nb, Sc)-substituted LLZO.[22,23,51]

For $Li_{6.45}Ga_{0.05}La_3Zr_{1.6}Ta_{0.4}O_{12}$, if we assume that all Ga was leached out to form the Li–Ga alloy and Li-ions were taken up from Li metal to keep the material neutral, the chemical formula of the reduced material would be $Li_{6.6}La_3Zr_{1.6}Ta_{0.4}O_{12}$, which should have a cubic phase as its major phase.[45] However, XRD analysis suggests that the reduced $Li_{6.45}Ga_{0.05}La_3Zr_{1.6}Ta_{0.4}O_{12}$ consists of a major phase in the tetragonal form. This indicates that at least one other element than Ga in $Li_{6.45}Ga_{0.05}La_3Zr_{1.6}Ta_{0.4}O_{12}$ would need to reduce its valence so that more Li-ions can be taken up. On the other hand, Zhu *et al.* proposed that the formation of the oxygen-deficient interphase due to the reduction of Zr^{4+} and Ta^{5+} in Ta-substituted LLZO by Li could stabilize the interface between Ta-substituted LLZO and Li to prevent Ta-substituted LLZO to reduce into the bulk.[22] The observation of $Li_{6.45}Ga_{0.05}La_3Zr_{1.6}Ta_{0.4}O_{12}$ being reduced into the bulk pellet also suggests that Ga in $Li_{6.45}Ga_{0.05}La_3Zr_{1.6}Ta_{0.4}O_{12}$ or $Li_{6.4}Ga_{0.2}La_3Zr_2O_{12}$ could possibly behave as Nb in Nb-substituted LLZO which segregates to the LLZO surface to destabilize the formation of the oxygen-deficient interphase, even with a relatively low amount of Ga-substitution in LLZO.

Conclusions

$Li_{6.4}Ga_{0.2}La_3Zr_2O_{12}$ and $Li_{6.45}Ga_{0.05}La_3Zr_{1.6}Ta_{0.4}O_{12}$ were synthesized by a solid state reaction for their stability tests toward Li. The reduction reaction propagation through bulk pellets can be directly observed by placing Ga-substituted LLZOs on a 250 °C heating plate. The EIS results show that $Li_{6.4}Ga_{0.2}La_3Zr_2O_{12}$ can be reduced by Li at 25 °C while $Li_{6.45}Ga_{0.05}La_3Zr_{1.6}Ta_{0.4}O_{12}$ seems to be stable to Li at 50 °C during the 60 days of experiment. ^{7}Li MAS NMR spectroscopy indicates that Li was infiltrated into the $Li_{6.4}Ga_{0.2}La_3Zr_2O_{12}$ bulk pellet during the reduction reaction, which should be a result of Li–Ga alloy formation due to the leaching out of Ga from the material structure as suggested by ^{71}Ga MAS NMR spectroscopy, which was also supported by the observation of high concentration Ga in the closed pores within $Li_{6.4}Ga_{0.2}La_3Zr_2O_{12}$ grains and by DFT calculations. When considering the low Ga concentration in $Li_{6.45}Ga_{0.05}La_3Zr_{1.6}Ta_{0.4}O_{12}$ together with the change from the cubic phase to the tetragonal phase from the XRD results, it is suggested that the segregation of Ga to the surface destabilizes the formation of the oxygen-deficient interphase and allows the reduction reaction to propagate through the bulk. The experimental results are in agreement with DFT calculations that the Ga-substituted LLZO/Li interface tends to transform into LLZO and Li_2Ga intermetallic compounds. The results highlight that the use of Ga-substituted LLZO as the solid electrolyte and Li as the anode for solid state battery development may not be feasible, even with a very low concentration of Ga substitution.

Experimental

LLZO samples were prepared *via* a four-step solid-state reaction. The starting materials $LiOH\cdot H_2O$ (Alfa Aesar, battery grade), La_2O_3 (Alfa Aesar, 99.9%, pre-dry at 900 °C for 10 h), ZrO_2 (Alfa Aesar, 99+%), Ta_2O_5 (Inframat, 99.9%) and Ga_2O_3 (Alfa Aesar, 99.999%) were mixed in stoichiometric amounts with 20 mol% $LiOH\cdot H_2O$ in excess. The prepared powder was dry milled by using a mortar grinder (Retsch, RM 200) incorporated with a tungsten carbide mortar and pestle for an hour. Then, the mixed powder was pressed into pellets for 20 h sessions of calcination, once at 850 °C and twice at 1000 °C. Grinding and pressing were repeated between the calcination steps. The sintering step of the ceramic pellets was carried out at 1175 °C with 30 hour dwell time. 7 g of calcined powder for each pellet was uniaxially pressed by using a 13 mm die under 150 MPa of pressure. After sintering, the pellets were sliced into thin discs by using a low-speed diamond saw (Minitom, Struers) for later applications. The materials prepared for this paper includes $Li_{6.4}Ga_{0.2}La_3Zr_2O_{12}$, $Li_{6.45}Ga_{0.05}La_3Zr_{1.6}Ta_{0.4}O_{12}$ and $Li_{6.45}Al_{0.05}La_3Zr_{1.6}Ta_{0.4}O_{12}$. The single crystals used for NMR studies were obtained by cleaning out the reduced $Li_{6.4}Ga_{0.2}La_3Zr_2O_{12}$ using absolute ethanol. $LiGaO_2$ was also prepared by a solid state reaction with one calcination step at 1000 °C for 10 hours of dwell time and one sintering step at 1175 °C for 10 hours of dwell time.

Powder X-ray diffraction (XRD) was carried out by using an EMPYREAN (Panalytical) with Ni-filtered Cu Kα radiation. Samples for XRD were collected from the sintered and reduced pellets by grinding and loading the ground powders into front loading sample holders. The diffractogramms were collected in the 2θ range from 10° to 80° at 40 kV, 40 mA, with a step size of 0.008° 2θ and counting time of 20 seconds per step. Qualitative

phase analysis was carried out with the QualX2.0 software package[52] employing the crystallography open database.[53–58] The phase compositions of the patterns were further analyzed within the GSAS II software package[59] by using a combined Le Bail/Rietveld approach.[60–62] Solid state nuclear magnetic resonance (NMR) spectra were acquired on a Bruker Advance NEO 800 MHz spectrometer using a 1.3 mm MAS probe spinning at 60 kHz with the Hahnecho pulse sequence. The 90° pulse length for ^{7}Li and ^{71}Ga was 1.6 and 1.5 μs, respectively. The recycle delay was 10 and 5 s, respectively. The 2D ^{7}Li exchange spectroscopy (EXSY) experiment was carried out with the mixing time in the range of 1 to 300 ms. ^{7}Li and ^{71}Ga shifts were referenced to LiF (−1 ppm) and $Ga_2(SO_4)_3$ (−87 ppm) powders. Microstructures and elemental chemistry distribution were investigated by using a Quanta 650 FEG scanning electron microscope (SEM) (FEI Company, USA) equipped with an energy dispersive spectrometer (EDS) (Ametek, USA).

EIS was used for determining the ionic conductivity of fabricated samples by using the Turnkey Broadband System Concept 80 (Novocontrol, Germany). The EIS measurements were done by using two different frequency generation systems. One used Agilent E4991B, which measured in the frequency range of 3 GHz ∼ 10 MHz, and the other used the Alpha-A analyzer, which measured in the frequency range of 10MHz ∼ 1 Hz, in the Broadband System Concept 80 system. Sputtered gold thin films were used as electrodes for ionic conductivity measurements. The impedance spectra were collected in the temperature range from −60 °C to 60 °C with a step size of 10 °C. For the stability studies of Li symmetric cells, a BioLogic VMP-300 multipotentiostat, combined with a climate chamber (Vötsch 4002 EMC), was used. The EIS data were analyzed by "ZView" (Scribner Associates, USA).

Density functional theory (DFT) calculations for Ga-substituted cubic LLZO and all possible competing compounds in Li–La–Zr–O–Ga are done by using the Vienna *Ab initio* Simulation Package (VASP).[63] The electron–ion interactions are evaluated by the projector augmented wave (PAW) method,[64] whereas the electron–electron interactions are calculated under exchange–correlation functional within the generalized gradient approximation of the Perdew–Burke–Ernzerhof method.[65] All atomic coordinates are relaxed until the total energy difference is smaller than 10^{-5} eV and the Hellmann–Feynman force on each atom is less than 0.01 eV Å^{-1}. The wave functions are built from the plane waves with a maximum energy cutoff of 520 eV, which is tested to achieve accuracy. The *k*-point mesh is set up as 2 × 2 × 2 for the 2 × 2 × 2 Ga-substituted LLZO supercell in the Monkhorst–Pack scheme and these *k*-point values might differ for other compounds depending on their cell sizes for converged formation energies. In this work, $Li_{6.25}Ga_{0.25}La_3Zr_2O_{12}$ ($Ga_{0.25}$-LLZO) and $Li_{6.625}Ga_{0.125}La_3Zr_2O_{12}$ ($Ga_{0.125}$LLZO) models are built for the rich and dilute Ga substitutions to match with our designed 2 × 2 × 2 cubic LLZO supercell. The reaction energies and equilibrated competing phases are determined by applying the self-developed Matlab code on all possible compounds of the Li–La–Zr–O–Ga system (ESI, Table S1†).

Author contributions

All authors made contributions to manuscript preparation and have given final approval for publication.

Conflicts of interest

There is no conflicts to declare.

Acknowledgements

This work was financially supported by the project of "US-German Cooperation on Energy Storage" under the funding programs of "LISI – Lithium Solid Electrolyte Interfaces" (Project No.: 13XP0224B) and "CatSe- Interfaces and Interphases in Rechargeable Li Based Batteries: Cathode/Solid Electrolyte" (Project No.: 13XP00223A) from the Bundesministerium für Bildung und Forschung (BMBF) and "High Performance Solid-State Batteries" (HIPSTER) from "Ministerium für Kultur und Wissenschaft des Landes Nordrhein-Westfalen". The authors also acknowledge the financial support from the Taiwan Ministry of Science and Technology (MOST) under the project No. 109-2636-E-006-012, 110-2636-E-006-016, 109-2923-E-006-006, and 110-2634-F-006-017.

References

1 C.-L. Tsai, S. Yu, H. Tempel, H. Kungl and R.-A. Eichel, *Mater. Technol.*, 2020, **35**, 656–674.
2 C. L. Tsai, V. Roddatis, C. V. Chandran, Q. Ma, S. Uhlenbruck, M. Bram, P. Heitjans and O. Guillon, *ACS Appl. Mater. Interfaces*, 2016, **8**, 10617–10626.
3 M. Balaish, J. C. Gonzalez-Rosillo, K. J. Kim, Y. Zhu, Z. D. Hood and J. L. M. Rupp, *Nat. Energy*, 2021, **6**, 227–239.
4 S. Lobe, C. Dellen, M. Finsterbusch, H. G. Gehrke, D. Sebold, C. L. Tsai, S. Uhlenbruck and O. Guillon, *J. Power Sources*, 2016, **307**, 684–689.
5 J. Sastre, X. Chen, A. Aribia, A. N. Tiwari and Y. E. Romanyuk, *ACS Appl. Mater. Interfaces*, 2020, **12**, 36196–36207.
6 J. Sastre, A. Priebe, M. Döbeli, J. Michler, A. N. Tiwari and Y. E. Romanyuk, *Adv. Mater. Interfaces*, 2020, **7**, 2000425.
7 S. Lobe, A. Bauer, S. Uhlenbruck and D. Fattakhova-Rohlfing, *Adv. Sci.*, 2021, **8**, e2002044.
8 L. Miara, A. Windmuller, C. L. Tsai, W. D. Richards, Q. Ma, S. Uhlenbruck, O. Guillon and G. Ceder, *ACS Appl. Mater. Interfaces*, 2016, **8**, 26842–26850.
9 Y. Ren, T. Liu, Y. Shen, Y. Lin and C.-W. Nan, *Journal of Materiomics*, 2016, **2**, 256–264.
10 K. Park, B.-C. Yu, J.-W. Jung, Y. Li, W. Zhou, H. Gao, S. Son and J. B. Goodenough, *Chem. Mater.*, 2016, **28**, 8051–8059.
11 C.-L. Tsai, Q. Ma, C. Dellen, S. Lobe, F. Vondahlen, A. Windmüller, D. Grüner, H. Zheng, S. Uhlenbruck, M. Finsterbusch, F. Tietz, D. Fattakhova-Rohlfing, H. P. Buchkremer and O. Guillon, *Sustainable Energy Fuels*, 2019, **3**, 280–291.

12 D. Rettenwander, J. Langer, W. Schmidt, C. Arrer, K. J. Harris, V. Terskikh, G. R. Goward, M. Wilkening and G. Amthauer, *Chem. Mater.*, 2015, **27**, 3135–3142.
13 D. Rettenwander, C. A. Geiger, M. Tribus, P. Tropper and G. Amthauer, *Inorg. Chem.*, 2014, **53**, 6264–6269.
14 B. Karasulu, S. P. Emge, M. F. Groh, C. P. Grey and A. J. Morris, *J. Am. Chem. Soc.*, 2020, **142**, 3132–3148.
15 C. Bernuy-Lopez, W. Manalastas, J. M. Lopez del Amo, A. Aguadero, F. Aguesse and J. A. Kilner, *Chem. Mater.*, 2014, **26**, 3610–3617.
16 M. A. Howard, O. Clemens, E. Kendrick, K. S. Knight, D. C. Apperley, P. A. Anderson and P. R. Slater, *Dalton Trans.*, 2012, **41**, 12048–12053.
17 J. F. Wu, E. Y. Chen, Y. Yu, L. Liu, Y. Wu, W. K. Pang, V. K. Peterson and X. Guo, *ACS Appl. Mater. Interfaces*, 2017, **9**, 1542–1552.
18 Y. Meesala, Y.-K. Liao, A. Jena, N.-H. Yang, W. K. Pang, S.-F. Hu, H. Chang, C.-E. Liu, S.-C. Liao, J.-M. Chen, X. Guo and R.-S. Liu, *J. Mater. Chem. A*, 2019, **7**, 8589–8601.
19 F. Han, Y. Zhu, X. He, Y. Mo and C. Wang, *Adv. Energy Mater.*, 2016, **6**, 1501590.
20 Y. Zhu, X. He and Y. Mo, *ACS Appl. Mater. Interfaces*, 2015, **7**, 23685–23693.
21 Y. Zhu, X. He and Y. Mo, *J. Mater. Chem. A*, 2016, **4**, 3253–3266.
22 Y. Zhu, J. G. Connell, S. Tepavcevic, P. Zapol, R. Garcia-Mendez, N. J. Taylor, J. Sakamoto, B. J. Ingram, L. A. Curtiss, J. W. Freeland, D. D. Fong and N. M. Markovic, *Adv. Energy Mater.*, 2019, **9**, 1803440.
23 D. Rettenwander, R. Wagner, A. Reyer, M. Bonta, L. Cheng, M. M. Doeff, A. Limbeck, M. Wilkening and G. Amthauer, *J. Phys. Chem. C*, 2018, **122**, 3780–3785.
24 R. Inada, K. Kusakabe, T. Tanaka, S. Kudo and Y. Sakurai, *Solid State Ionics*, 2014, **262**, 568–572.
25 P. R. Mercier, J.-P. Malugani and B. F. e. G. Robert, *Acta Crystallogr., Sect. B: Struct. Crystallogr. Cryst. Chem.*, 1982, **38**, 1887–1890.
26 V. Lacivita, N. Artrith and G. Ceder, *Chem. Mater.*, 2018, **30**, 7077–7090.
27 M. O. Schmidt, M. S. Wickleder and G. Meyer, *Z. Anorg. Allg. Chem.*, 1999, **625**, 539–540.
28 A. Sharafi, E. Kazyak, A. L. Davis, S. Yu, T. Thompson, D. J. Siegel, N. P. Dasgupta and J. Sakamoto, *Chem. Mater.*, 2017, **29**, 7961–7968.
29 D. Rettenwander, G. Redhammer, F. Preishuber-Pflugl, L. Cheng, L. Miara, R. Wagner, A. Welzl, E. Suard, M. M. Doeff, M. Wilkening, J. Fleig and G. Amthauer, *Chem. Mater.*, 2016, **28**, 2384–2392.
30 R. Wagner, G. J. Redhammer, D. Rettenwander, A. Senyshyn, W. Schmidt, M. Wilkening and G. Amthauer, *Chem. Mater.*, 2016, **28**, 1861–1871.
31 C. Chen, Y. Sun, L. He, M. Kotobuki, E. Hanc, Y. Chen, K. Zeng and L. Lu, *ACS Appl. Energy Mater.*, 2020, **3**, 4708–4719.
32 S. Qin, X. Zhu, Y. Jiang, M. 'en Ling, Z. Hu and J. Zhu, *Appl. Phys. Lett.*, 2018, **112**, 113901.
33 W. Lan, H. Fan, V. W.-h. Lau, J. Zhang, J. Zhang, R. Zhao and H. Chen, *Sustainable Energy Fuels*, 2020, **4**, 1812–1821.
34 M. Kim, G. Kim and H. Lee, *Micromachines*, 2021, **12**, 134.
35 C. Li, Y. Liu, J. He and K. S. Brinkman, *J. Alloys Compd.*, 2017, **695**, 3744–3752.
36 H. El Shinawi and J. Janek, *J. Power Sources*, 2013, **225**, 13–19.
37 L. Buannic, B. Orayech, J.-M. López Del Amo, J. Carrasco, N. A. Katcho, F. Aguesse, W. Manalastas, W. Zhang, J. Kilner and A. Llordés, *Chem. Mater.*, 2017, **29**, 1769–1778.
38 J. L. Allen, J. Wolfenstine, E. Rangasamy and J. Sakamoto, *J. Power Sources*, 2012, **206**, 315–319.
39 J. Wolfenstine, J. Ratchford, E. Rangasamy, J. Sakamoto and J. L. Allena, *Mater. Chem. Phys.*, 2012, **134**, 571–575.
40 X. Xiang, F. Chen, Q. Shen, L. Zhang and C. Chen, *Mater. Res. Express*, 2019, **6**, 085546.
41 M. Yi, T. Liu, J. Li, C. Wang, Y. Mo, X. Wang and Y. Wei, *J. Solid State Electrochem.*, 2019, **23**, 1249–1256.
42 F. M. Pesci, A. Bertei, R. H. Brugge, S. P. Emge, A. K. O. Hekselman, L. E. Marbella, C. P. Grey and A. Aguadero, *ACS Appl. Mater. Interfaces*, 2020, **12**, 32806–32816.
43 J. Su, X. Huang, Z. Song, T. Xiu, M. E. Badding, J. Jin and Z. Wen, *Ceram. Int.*, 2019, **45**, 14991–14996.
44 M. Philipp, B. Gadermaier, P. Posch, I. Hanzu, S. Ganschow, M. Meven, D. Rettenwander, G. J. Redhammer and H. M. R. Wilkening, *Adv. Mater. Interfaces*, 2020, **7**, 2000450.
45 E. Rangasamy, J. Wolfenstine and J. Sakamoto, *Solid State Ionics*, 2012, **206**, 28–32.
46 M. Rawlence, A. N. Filippin, A. Wackerlin, T. Y. Lin, E. Cuervo-Reyes, A. Remhof, C. Battaglia, J. L. M. Rupp and S. Buecheler, *ACS Appl. Mater. Interfaces*, 2018, **10**, 13720–13728.
47 X. Xie, J. Xing, D. Hu, H. Gu, C. Chen and X. Guo, *ACS Appl. Mater. Interfaces*, 2018, **10**, 5978–5983.
48 S.-k. Lin and S.-w. Chen, *J. Mater. Res.*, 2006, **21**, 1712–1717.
49 S. Tamura, K.-i. Araki and N. Imanaka, *Journal of Asian Ceramic Societies*, 2018, **4**, 390–393.
50 Y. Kobayashi, T. Egawa, S. Tamura, N. Imanaka and G.-y. Adachi, *Chem. Mater.*, 1997, **9**, 1649–1654.
51 H. Nemori, Y. Matsuda, S. Mitsuoka, M. Matsui, O. Yamamoto, Y. Takeda and N. Imanishi, *Solid State Ionics*, 2015, **282**, 7–12.
52 A. Altomare, C. Cuocci, C. Giacovazzo, A. Moliterni and R. Rizzi, *J. Appl. Crystallogr.*, 2008, **41**, 815–817.
53 A. Merkys, A. Vaitkus, J. Butkus, M. Okulic-Kazarinas, V. Kairys and S. Grazulis, *J. Appl. Crystallogr.*, 2016, **49**, 292–301.
54 M. Quiros, S. Grazulis, S. Girdzijauskaite, A. Merkys and A. Vaitkus, *J. Cheminf.*, 2018, **10**, 23.
55 A. Vaitkus, A. Merkys and S. Grazulis, *J. Appl. Crystallogr.*, 2021, **54**, 661–672.
56 S. Grazulis, D. Chateigner, R. T. Downs, A. F. Yokochi, M. Quiros, L. Lutterotti, E. Manakova, J. Butkus, P. Moeck and A. Le Bail, *J. Appl. Crystallogr.*, 2009, **42**, 726–729.
57 S. Grazulis, A. Daskevic, A. Merkys, D. Chateigner, L. Lutterotti, M. Quiros, N. R. Serebryanaya, P. Moeck, R. T. Downs and A. Le Bail, *Nucleic Acids Res.*, 2012, **40**, D420–D427.
58 S. Grazulis, A. Merkys, A. Vaitkus and M. Okulic-Kazarinas, *J. Appl. Crystallogr.*, 2015, **48**, 85–91.

59 B. H. Toby and R. B. Von Dreele, *J. Appl. Crystallogr.*, 2013, **46**, 544–549.
60 A. Le Bail, *Powder Diffr.*, 2012, **20**, 316–326.
61 H. M. Rietveld, *Phys. Scr.*, 2014, **89**, 098002.
62 H. M. Rietveld, *J. Appl. Crystallogr.*, 1969, **2**, 65–71.
63 G. Kresse and D. Joubert, *Phys. Rev. B*, 1999, **59**, 1758.
64 P. E. Blöchl, *Phys. Rev. B: Condens. Matter Mater. Phys.*, 1994, **50**, 17953.
65 J. P. Perdew, K. Burke and M. Ernzerhof, *Phys. Rev. Lett.*, 1996, **77**, 3865.